Study of Kirkpatrick-Baez X-ray optics made with Silicon Pore Optics for full-field X-ray fluorescence microscope

Gnezdovskaia, Nelli

Study of Kirkpatrick-Baez X-ray optics made with Silicon Pore Optics for full-field X-ray fluorescence microscope

THESIS

submitted in partial fulfillment of the
requirements for the degree of

MASTER OF SCIENCE
in
PHYSICS

Author :	N. Gnezdovskaia
Student ID :	2874253
Supervisor :	Dr. M.J.A. de Dood
Second corrector :	Dr. N. Barrière

Leiden, The Netherlands, July 18, 2022

Study of Kirkpatrick-Baez X-ray optics made with Silicon Pore Optics for full-field X-ray fluorescence microscope

N. Gnezdovskaia

Huygens-Kamerlingh Onnes Laboratory, Leiden University
P.O. Box 9500, 2300 RA Leiden, The Netherlands

July 18, 2022

Abstract

This works investigates the possibility of building a full-field X-ray fluorescence microscope using Silicon Pore Optics (SPO) technology in the Advanced Kirkpatrick-Baez (AKB) configuration. AKB system focuses the X-ray beam by reflection from four curved mirrors. Such an imaging system is an aberration-free and relatively easy to manufacture optics.
We start with a simple two-mirror Kirkpatrick-Baez (KB) system as a first step and a basis for understanding and modelling of Advanced KB. Using the derived equations, a KB system is parameterized and characterized. A sensitivity study is conducted to find the optimal system parameters under constraints enforced by microscopy application and SPO technology. Performance of an optical system is assessed on the basis of solid angle, tightness of focal spot and field of view. The conclusions made for the KB system are relevant for the AKB system as well.
SPO technology was initially developed to enable light-weight large area telescopes with resolution of a few arc seconds. It uses the concept of stacking of slightly curved reflective mirrors of high quality. We were interested to explore whether SPO can improve X-ray microscopy. However, it was found that using SPO technology for the case of full-field X-ray microscopy presents no benefits in terms of increase of solid angle. Nonetheless, the technology can be used to provide self-standing stacks with only upper reflecting plate for AKB-based microscopy setup.

Contents

Chapter 1

Introduction

Starting from their discovery, X-rays were expected to create an impact in the area of microscopy and imaging of the objects traditionally opaque in the visible region. Elements have fluorescence lines in X-rays, which allow identifying their presence and locating them in the sample. Scientists have been working on building an understanding of this type of radiation and developing various types of X-ray microscopes. In X-ray fluorescence microscopy atoms are excited by an intense beam of X-rays, and their fluorescence is observed. Among the X-ray fluorescence microscopes are scanning [1, 2], lensless (coherent x-ray diffraction) [3, 4] and full-field [5, 6] microscopes. However, a high-resolution X-ray fluorescence microscope is still under development due to the challenges in production of the X-ray focusing optics free of aberrations.

Full-field X-ray fluorescence microscopy (FXFM) is currently the most exciting compared to other types with their clear disadvantages. For example, scanning microscopy is able to provide spatial resolution of order of 30 nm [1]. In spite of that, such resolution strongly depends on precision of the mechanical sample positioners. Moreover, since high resolution requires many scanning steps, it could take considerable amount of time between two spots in the beginning and the end of the scanning run. For highly dynamic systems this could lead to erroneous results [7]. On the contrary, FXFM allows to obtain a fluorescence map of the sample at one glance, hence, detecting all parts of it simultaneously.

Although full-field X-ray microscopy does not require fine sample positioners, it does require an optical imaging system capable of doing the job. Several candidates, existing at the moment, are Fresnel zone plates [5], refractive lenses [6], Wolter mirrors [8] and (advanced) KirkpatrickâBaez (KB) mirrors [9]. The first two of them, based on the principles of diffrac-

tion and refraction, inevitably produce chromatic aberrations. The last two are free from this type of aberrations, employing total external reflection as a main principle. However, Kirkpatrick-Baez mirrors are subjects to coma aberrations, which degrade the resulting image quality. Wolter optical design is free from chromatic and coma aberrations and so far is considered to be the most suitable imaging design. The significant drawback of this type of optics is a difficulty in production of the reflecting surfaces of the required quality.

One more candidate for FXFM was proposed by Kodama [10]. The concept, called Advanced Kirkpatrick-Baez (AKB) system, uses two pairs of KB mirrors and is able to provide aberration-free high-resolution imaging. It was shown in literature that AKB-based full-field X-ray microscopes can provide decent spatial resolution: Matsuyama *et al.* [7] reported a half-period spatial resolution of around 0.5 - 1 μm, Yamada *et al.* [11] were able to resolve 100-nm periods (50-nm line widths) at X-ray energy of 15 keV.

Silicon Pore Optics (SPO) technology [12] is a method of manufacturing stacks of slightly curved mirrors, enabling to enlarge the collection area of telescopes. We are interested in the idea of combining the two latter mentioned methods, AKB optics and SPO technology, to possibly improve full-field X-ray microscopy in terms of increase of solid angle and collection area.

The goal of this thesis is to study the possibility of building a full-field X-ray microscope combining the Advanced Kirkpatrick-Baez (AKB) system of four mirrors with the Silicon Pore Optics technique. Starting with the traditional two-mirror Kirkpatrick-Baez (KB) system as a stepping stone, we develop an understanding which applies to an advanced system as well. The study is structured as follows:

- Literature review;
- Deriving the equations for KB system;
- Exploring options for modelling of a KB system:
  - First, using Zemax to get the first understanding of the system;
  - Second, switching to a more advanced and powerful X-ray tracing tool - XRT python library;
- Optimization of the KB system;
- Investigation of a SPO stack for (A)KB configuration;
- Conclusions and Outlook.

Chapter 2

An overview of the X-ray focusing optics

2.1 Introduction

X-ray is a high-energy electromagnetic radiation which was discovered by W.C. Röntgen in 1895 [13]. It is characterized by energies in the range from 100 eV to 100 keV and the corresponding wavelengths from approximately 0.01 nm to 10 nm. X-rays have penetrating nature, and this ability of X-rays is determined by the photon energy and the density of material. The higher the density, the lower penetration length and the higher absorption by the material [14].

Being a breakthrough in the microscopy field, the X-rays present a significant challenge in the area of focusing optics. This type of radiation can not be focused using the conventional glass lenses, how it is done for visible light. The refractive index depends on the wavelength of light, and in the case of X-rays refractive index of most materials is below but very close to unity [15]. That is why the most common way to focus X-rays is to employ a phenomenon of total external reflection at grazing incidence (see more details in Section 2.2).

Despite the above mentioned difficulties, X-rays possesses the advantageous qualities, which encourage scientists to keep pursuing X-ray research. Due to its short wavelength, X-ray-based microscopes allow to provide significantly higher resolution than those using visible light sources. In addition, X-ray microscopes can work with unaltered samples, whereas high-resolution electron microscopes require significant sample preparation. The penetration ability of X-rays makes it possible to capture the

internal features of the sample without its destruction. Thus, X-ray microscopy is a perfect combination of sufficiently good resolution, depth of field and sample manipulation.

2.2 X-ray focusing optics characteristics

This section discusses the characteristics of X-ray focusing optics such as sagittal and meridional curvatures and the most common types of aberrations (coma, spherical, astigmatism).

The most common technique to redirect X-rays is implementing the phenomenon of total external reflection at shallow grazing [1] incidence angle. Similar to total internal reflection, X-rays propagate in air or vacuum (n = 1) and at small grazing angles ('grazing incidence') reflect from the surface of a highly dense material with $n < 1$, e.g. a silicon wafer with reflective coating.

2.2.1 Sagittal and meridional radii

For the purpose of X-ray focusing it is important that the reflecting mirror is curved. In an aspherical surface there are two types of radii of curvature present - sagittal and meridional radii. Figure 2.1 shows the planet Earth with both radii marked. Upon the full rotation around the axis of revolution, meridional radius results in producing the complete surface of Earth. The sagittal radius (parallel to the equator) upon rotation only produces a planar slice of the volume.

2.2.2 Aberrations

The focusing optics often suffer from optical aberrations leading to distorted or blurred images on the detector. Here we consider the most common types of aberrations occurring in X-ray imaging.

Spherical aberrations

Spherical aberrations are typical for optical elements with spherical surfaces. When a bundle of parallel beams is falling onto a lens with spherical aberrations, only the central part of the lens focuses the light into the focus

[1] Grazing angle is an angle between the beam and the surface tangent.

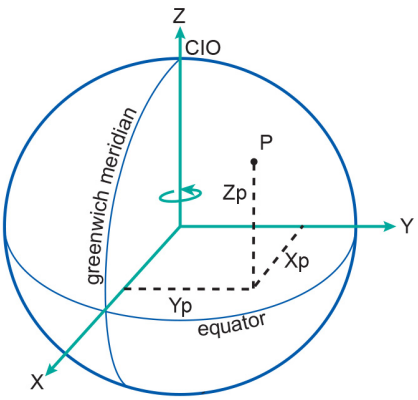

Figure 2.1: *Schematic representation of the coordinate system of the Earth. The Earth's axis of rotation, Greenwich meridian and equator are shown. Credit: [16]*

point. The edges of the lens bend the incoming light either too much (positive spherical aberration) or not enough (negative spherical aberration), thereby leading to the formation of the 'bull's eye' (see Figure 2.2) [17].

Coma aberrations

Typically when light strikes the focusing system, it is focused at one point. However, if the system suffers from coma aberrations, this will be valid only for the beams coming parallel to the optical axis of the system. Beams coming at an angle (e.g. from off-axis sources) produce a distorted 'comet-shaped' distribution (see Figure 2.2) [17].

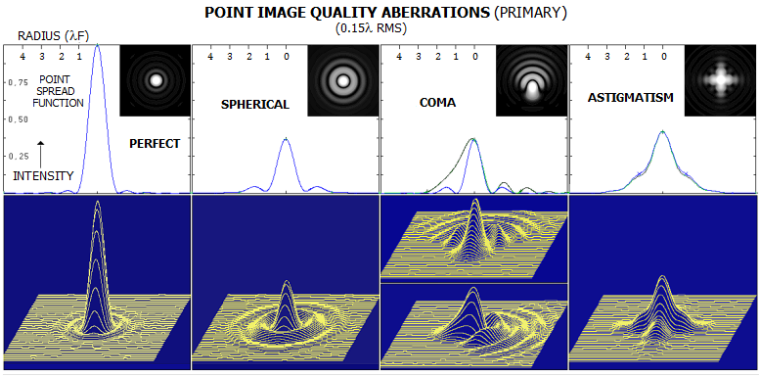

Figure 2.2: *The point spread function of the perfect point source and of the system with spherical aberrations, coma aberrations and astigmatism. Credit: [17].*

Astigmatism

As each surface has meridional and sagittal radii, it also has the corresponding planes. The meridional plane contains both the optical axis of the system and the chief ray, and the sagittal plane is perpendicular to the meridional plane and contains only the chief ray. A system with astigmatism has different foci in the sagittal and meridianal planes. Hence, depending on the position on the optical axis, the formed image will be an ellipsoid, stretched in either sagittal or meridional planes, or a circle of the least confusion in between the two foci [18]. The overall image of the point source is shown in Figure 2.2.

Astigmatism, spherical and coma aberrations are the examples of the wave-front aberrations. They produce the deformation of the wave front and the subsequent redistribution of energy in the system, leading to ray aberrations [19].

2.3 Designs of focusing optics

This section provides a discussion of the most common designs of X-ray focusing optics, based on the principle of total external reflection at grazing incidence.

2.3.1 Kirkpatrick-Baez Optics

The first attempt to provide a solution for X-ray focusing was made by P. Kirkpatrick and A.V. Baez in 1948 [9]. The proposed arrangement consists of two aspherical mirrors oriented perpendicularly. Light, propagating at shallow grazing angle to the mirror surface, undergoes total external reflection from both surfaces. The first reflection focuses the incident light into a line (vertical or horizontal, depending on the orientation of the first mirror), which is subsequently focused to the focal point of the system with the second reflection (see Figure 2.3). Various types of asperical reflective surfaces can be used: parabolic surface is used to collimate beams, elliptical - to focus beams [20].

One of the main advantages of Kirkpatrick-Baez (KB) optics is the ease in manufacturing and relative cheapness. This type of optics is suitable for nesting (multi-mirror system). This means the utilization of multiple thin reflecting surfaces, which allows to increase the aperture.

Employing only reflection (and not refraction or diffraction), Kirkpatrick-Baez optics is free of chromatic aberrations. However, a serious drawback

of KB optics is the presence of coma aberrations (single reflection can not satisfy the Abbe condition), which reduces both resolution and field of view [20, 21].

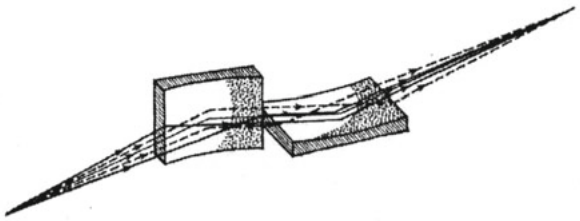

Figure 2.3: *The Kirkpatrick-Baez X-ray focusing system, containing two perpendicularly oriented mirrors. Credit: [20].*

2.3.2 Wolter Optics

An optics, able to satisfy the Abbe condition[2], was proposed in 1952 by H. Wolter [23]. There are three types of Wolter optics, which all consist of two curved mirrors. Wolter types 1 and 2 use hyperbolic and parabolic surfaces, and Wolter type 3 uses parabolic and elliptical mirrors (see Figure 2.5a, b, c). Wolter optics of type 1 (Wolter-1) is the most common as it is well suited for 'nesting'. Multiple thin reflecting surfaces are inserted one inside another and form the construction concentrically oriented to the optical axis (See Figure 2.5d). Such a multi-mirror arrangement allows to increase the effective collection area, which is crucial for observing typically weak X-ray sources.

Wolter designs were initially developed for X-ray astronomy applications. Now Wolter-1 optics is a basis for Silicon Pore Optics technology, which was invented by cosine Research company in collaboration with Europien Space Agency (ESA) [12] for implementing in ATHENA telescope. Silicon wafers, with reflecting coating on one side and with multiple ribs on the other side, are stacked together, forming a porous construction. The optical axis of the system is oriented along the ribs (along the meridional curvature). X-rays, incident on each of the pores, are reflected by the two mirrors and focused at the focal point, where the detector is located. Four stacks, assembled together, form a mirror module, which is

[2]The Abbe sine condition [22] is a condition that must be satisfied by the optical system in order for it to produce sharp images of off-axis as well as on-axis objects.

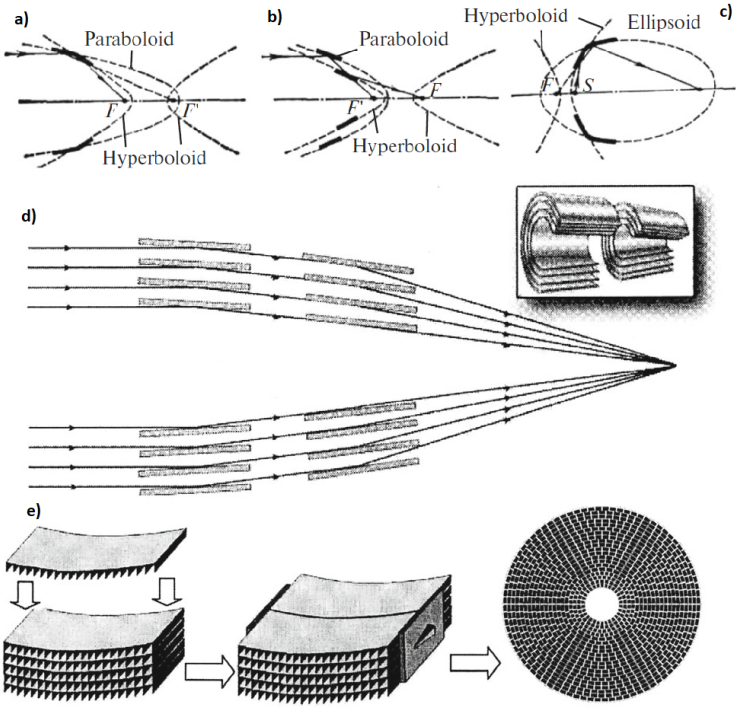

Figure 2.4: *The Wolter optics designs of type 1 (a), 2 (b) and 3 (c). The nested design of the Wolter-1 optic (d). The Silicon Pore Optics technique (e): stacking of the silicon plates with ribs, assembling of the mirror modules for the ATHENA telescope. Credit [20].*

the simplest optical element of the future ATHENA telescope (see Figure 2.5e).

Wolter optics is practically an ideal candidate for the X-ray focusing optics role. With fairly good accuracy, it satisfies Abbe sine condition. This optical system does not suffer from astigmatism, spherical, coma or chromatic aberrations [21] and allows for diffraction-limited resolution in case of the sufficiently high accuracy of the mirror fabrication. However, making Wolter mirrors of relatively small radii of curvature, as required for microscopy, is extremely difficult and remains nowadays impossible with high quality.

2.3.3 Advanced Kirkpatrick-Baez Optics

In 1996 Kodama *et al.* proposed an improved optical design for X-ray focusing - advanced Kirkpatrick-Baez (AKB) optics [10]. The system consists of two sets of Kirkpatrick-Baez mirrors (four mirrors in total) and allows

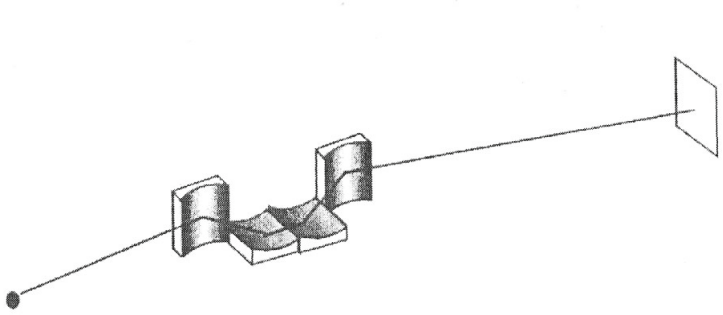

Figure 2.5: *The example configuration of the advanced Kirkpatrick-Baez optical system. Credit: [20].*

for various configurations depending on the purpose. For the full-field X-ray microscopy elliptical and hyperbolic surfaces are well suited [20, 21].

AKB optics provides a good focusing solution and comprises the easy manufacturing property of the KB mirrors and all the benefits of the Wolter optics. It satisfies the Abbe sine condition and is free from coma, wavefront and chromatic aberrations [20]. In addition, it allows to achieve diffraction-limited resolution. However, a high degree of freedom in such a system can introduce a difficulty in adjusting and stabilizing it.

Chapter 3

Simple KB system

3.1 Introduction

The classical Kirkpatrick-Baez system consists of two orthogonal curved mirrors, each focusing in one direction (horizontal or vertical). In general, the mirrors in the system can be parabolic, elliptical or hyperbolic, including any their combinations. The specific type of curved surfaces used depends on the purpose. Parabolic mirrors work well to focus a parallel beam or to collimate a diverging beam. Elliptical mirrors are used to focus a diverging beam. For the case of a microscopy setup, we are interested to have the same focusing properties in both horizontal and vertical directions and, hence, choose to use the same type of curved mirrors. Another requirement of microscopy is focusing of the diverging beam coming from the exposed sample, which is satisfied by using two elliptical mirrors in the KB system.

3.2 Theoretical description and modeling of the system

3.2.1 System with one elliptical mirror

3.2.1.1 Defining the system

Let us consider an optical system constrained by an ellipse lying in the YZ-plane. The optical axis of the system is directed along Y-axis and coincide with the semi-major axis of ellipse. The mirror is curved in the meridional direction (along the optical axis) being a part of the ellipse's surface (see

Figure 3.1). At the same time, the sagittal radius of the mirror is infinite (plane). The parameters, fully defining the ellipse, are semi-major distance a, semi-minor distance b and ellipse's center-to-focus distance c. A useful characteristic of ellipse is eccentricity $\epsilon = c/a$, showing how prolate an ellipse is. The X-ray source and detector screen are located on the optical axis at the focal points of the ellipse, corresponding to $[0, 0, 0]$ and $[0, 2c, 0]$. The center of the ellipse is shifted from the origin of the coordinate system by the focal length. The ellipse follows the equation:

$$\frac{(y-c)^2}{a^2} + \frac{z^2}{b^2} = 1, \tag{3.1}$$

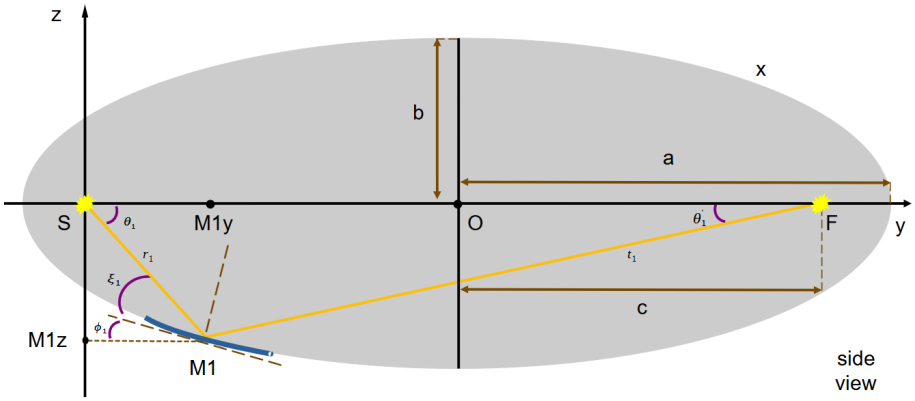

Figure 3.1: *A schematic representation of an ellipse with parameters a (half-length), b (half-width) and c (half-distance between foci S and F) in YZ coordinate plane. An elliptical mirror (M1) is shown in blue.*

3.2.1.2 System parametrization

We choose to parametrize our system with:

- the grazing[1] angle on the first mirror, taken in the middle of the mirror,
- the total system length SF (the distance between the source and the detector),
- the magnification of the image on the detector screen produced by mirror M1,

[1]Grazing angle is equal to the difference between $\pi/2$ and incidence angle.

- the lengths of mirror projected on the Y-axis and X-axis (the mirror has rectangular shape of size (L_x, L_y)).

The mirror is only curved in the meridional plane (along Y-direction). The resulting curvature in the center of the mirror is at least several meters. For the mirror length less than 10% of the mirror curvature we can safely assume that the mirror length is approximately equal to the length projection on Y-axis. From the input parameters we define all the rest parameters of the system. The mirror's parameters apply to its center. For one mirror, the parameters are:

- Position along X, Y, Z: M1x, M1y, M1z,
- Rotations along X, Y, Z (pitch, roll and yaw): $-\phi_1$, 0 and θ_2,
- Dimensions of the mirror: length L_y and Width L_x,
- Radii of curvature,
- Sag (calculated from the length and curvature).

The total system length SF equals to the distance $2c$, connecting the two foci. Magnification m_1 of the system in the vertical direction is given by the ratio of the distances from the center of M1 to detector (t_1) and from the source to the center of M1 (r_1) in YZ-plane. By substituting the dependence $t_1 = m_1 \cdot r_1$ into the law of cosine for the triangle SM_1F: $(2c)^2 = {r_1}^2 + {t_1}^2 - 2r_1t_1cos(\pi - 2\xi_1)$, we find $r_1 = 2c/\sqrt{1 + {m_1}^2 - 2m_1cos(\pi - 2\xi_1)}$. The sum of the distances r_1 and t_1 equals to the double semi-major axis: $r_1 + t_1 = 2a$. Using the derived ellipse parameters, we obtain the eccentricity ϵ as c/a and the semi-minor axis b as $\sqrt{a^2(1-\epsilon^2)}$.

Any radius-vector $r(\theta)$, connecting a focus point with the point belonging to ellipse, can be found through angular coordinate:

$$r(\theta) = \frac{a(1-\epsilon^2)}{1 \pm \epsilon cos(\theta)}, \tag{3.2}$$

where the sign in denominator depends on the direction of $r(\theta)$: negative if pointing towards the center and positive otherwise. From equation 3.3, knowing $r_1 = r(\theta)$, an absolute source pitch angle θ_1 can be calculated. The pitch angle of mirror M1 is $\phi_1 = \theta_1 - \xi_1$. The Y-coordinate of M1 is found from the right triangle as $SM_{1y} = r_1cos(\theta_1)$. The Z-coordinate ($SM_{1z}$) can be found using equation (deduced from equation 3.1):

$$z = \pm \frac{b}{a} \sqrt{a^2 - (y - c)^2}, \tag{3.3}$$

with $y = SM_{1y}$.

3.2.2 System with two elliptical mirrors

3.2.2.1 Defining the system

In KB design we consider the system of two elliptical mirrors (see Figure 3.2). Each mirror is a part of one of the two ellipses located in perpendicular planes: the first in ZY-plane (M1), and the second in XY-plane (M2). The two ellipses are identical and share the same focal points. Similarly to the case of one mirror, the optical axis of the two-mirror system coincides with the major axis of the ellipses, being Y-axis. As previously, source and detector are located on the optical axis in the focal points of ellipses, which correspond to $[0, 0, 0]$ and $[0, 2c, 0]$. The common center of the two ellipses in our coordinate system is shifted from origin by the focal length c.

All the calculations in Section 3.2.1 apply to the second mirror, simply replacing the Z-coordinate by X.

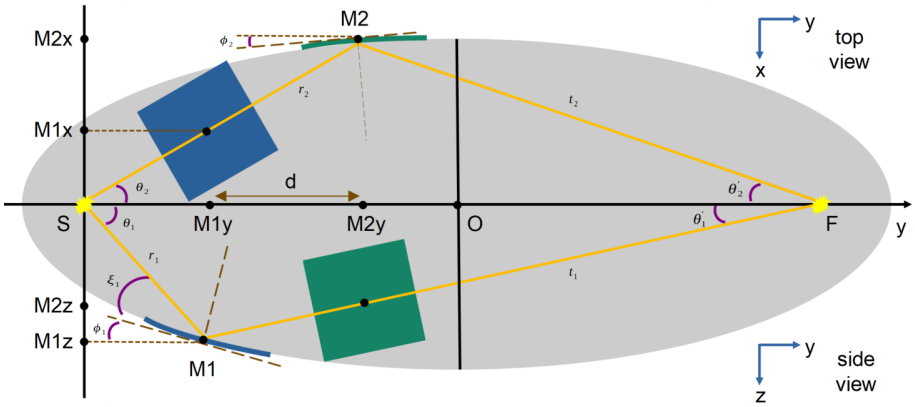

Figure 3.2: *A schematic representation of two elliptical mirrors system. In two planes (YX - top view and YZ - side view) ellipses describing the system match and share the focal points where source and detector are located.*

3.2.2.2 System parametrization

The parametrization of the system includes the input parameters previously stated in Section 3.2.1.2 and, additionally, the distance d ($d \geq L_y$) between the two mirrors.

In this case the magnification is calculated in a slightly different way. Adding the second mirror to the system means that the mirrors need to be shifted from the optical axis (see detailed explanation below). This fact forces us to work with the vector representation of the rays and not just projections. The two reflection optical system implies three vector directions: source to mirror M1 ($\vec{d_1}$), M1 to M2 ($\vec{s_{12}}$) and M2 to detector ($\vec{f_2}$). The approximate magnifications can be found as in Section 3.2.1.2: $m_{1,2} = t_{1,2}/r_{1,2}$ (with the corresponding index), where r_1 and t_1 are the projections of $\vec{d_1}$ and $\vec{s_{12}} + \vec{f_2}$ in YZ-plane, and r_2 and t_2 are the projections of $\vec{d_1} + \vec{s_{12}}$ and $\vec{f_2}$ in XY-plane. To get real magnifications of the system we need to take into account the distances of the three 3D vectors. Magnification produced by the first mirror (in the vertical plane) is $m_1^{real} = \frac{|\vec{s_{12}}|+|\vec{f_2}|}{|\vec{d_1}|}$ and by the second mirror (in the horizontal plane) is $m_2^{real} = \frac{|\vec{f_2}|}{|\vec{d_1}|+|\vec{s_{12}}|}$. For a large system (with the source to detector distance more than a few meters), the corresponding approximate and real magnifications are very close. The real focal distance of the ellipse is also affected by the shift from the optical axis. The double focal length of ellipse is calculated as the projection of the vector $\vec{d_1} + \vec{s_{12}} + \vec{f_2}$ on the Y-axis.

The input distance between mirrors implies Y-coordinate of the center of the mirror M2 as $SM_{2y} = SM_{1y} + d$, X-coordinate (SM_{2x}) can be found using equation (3.3) by replacing z with x and with $y = SM_{2y}$.

Each of the mirrors, being a part of the corresponding ellipse, is shifted from the optical axis in one of the planes: M1 is shifted along Z-axis and M2 - along X-axis. In order to make the system work, each of the mirrors also needs to be shifted in the direction perpendicular to the plane of the corresponding ellipse. Thereby, for the first mirror we introduce a non-zero shift along X-axis by SM_{1x} and for the second mirror a non-zero shift along Z-axis by SM_{2z}. Each of the mirrors is rotated by a certain yaw angle such that the axis of the mirror M1 is parallel to r_2 and the axis of the mirror M2 is parallel to t_1. The yaw angle of M1 equals to the yaw angle of the source and is calculated as $\theta_2 = arctan(SM_{2x}/SM_{2y})$. This allows to calculate X-coordinate of the center of M1: $SM_{1x} = SM_{1y} \cdot tan(\theta_2)$. The yaw angle of M2 equals to $\theta_1^{'} = arcsin(\sqrt{(r_1^2 + {SM_{1y}}^2)}/t_1)$, and we find the absolute Z-shift of the second mirror $SM_{2z} = (SF - SM_{2y}) \cdot tan(\theta_2^{'})$. By finding angles $\theta_2^{'} = arctan(SM_{2x}/(SF - SM_{2y}))$ and $SM_2F = 180 - (\theta_2 + \theta_2^{'}) \cdot 180/\pi$ (in degrees) we calculate a pitch angle of M2: $\phi_2 = (90 - (\frac{1}{2}SM_2F + \theta_2^{'} \cdot 180/\pi)) \cdot \pi/180$ (in radians).

The resulting coordinates of the center of mirror 1 are $[-SM_{1x}, SM_{1y}, -SM_{1z}]$ and of mirror 2 are $[-SM_{2x}, SM_{2y}, -SM_{2z}]$. The M1 pitch and yaw angles are $-\phi_1$ and θ_2, correspondingly. The M2 pitch, roll and yaw angles are $-\phi_2$, $\pi/2$ and $\theta_2^{'}$, correspondingly. The source has a pitch angle of $-\theta_1$ and yaw angle of θ_2.

3.2.2.3 Widths of mirrors

The beam coming from the point source S expands and reaches the maximum divergence on the surface of the second mirror. The maximum divergence of the source beam in XY-plane (marked as $divergence_x$ in Figure 3.3) is estimated as an angle between the extreme vector rays hitting mirror 2 of length L_y. The same vectors define the width L_{x1} of mirror 1. The effective width of M1 (shown as red rectangle in the top XY-plane in Figure 3.3) is chosen such that it collects the whole bunch of diverging rays. We calculate it as an intersection of the outer rays with the plane, located at the right edge of M1 and oriented perpendicular to the ray, coming straight to the center of M2 from the source.

Similarly, the divergence of the source beam in YZ-plane (marked as $divergence_z$ in Figure 3.3) is defined by length L_y of mirror 1 and calculated as an angle between the extreme vectors hitting M1. The beam reflected from the mirror 1 is converging towards the detector plane in point F. The effective width L_{x2} of mirror 2 is shown as a red rectangle in the bottom YZ-plane in Figure 3.3. It is calculated as distance between the points of intersection of the extreme rays, reflected from the center of M1 and directed to the detector F, with the plane located at the left edge of M2 and oriented perpendicular to the central ray, coming from M1 to the detector.

3.2.2.4 Characterization of the system

The system is characterized by the following parameters:

- Vertical / horizontal magnification (calculated);
- Entrance pupil and related solid angle (calculated);
- Centroid is a measure to assess where the data distribution is centered. We calculate it as an average between maximum and minimum values of data array in each of X-, Y- and Z-directions.
- Half-energy width (HEW) of a data distribution - diameter of the circle, comprising half of the rays in distribution;

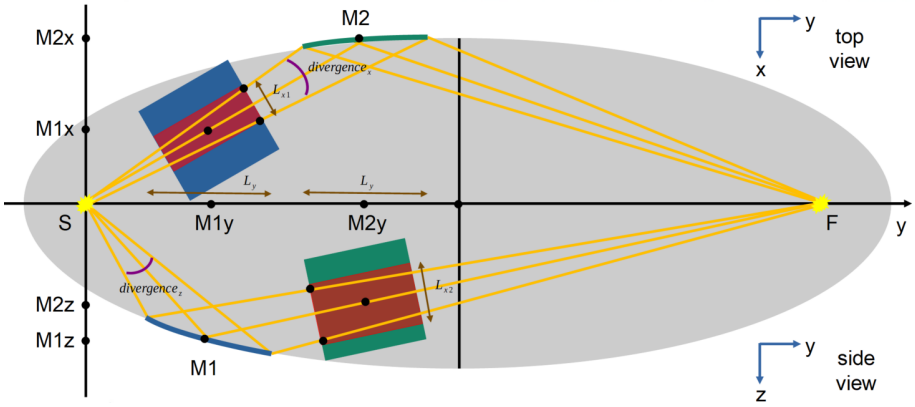

Figure 3.3: *A schematic representation of the formation of the lengths L_{x1} and L_{x2} as well as the beam divergences $divergence_x$ and $divergence_z$.*

- Field of view (FOV) - characterizes maximal shift of the source from the optical axis, when the resulting image on the detector is of relevant quality (when HEW degrades by up to 100x times [2]). Obtained from ray trace simulation;
- Throughput - shows how many photons successfully reach the detector after reflection from all the surfaces within the optical system.

3.2.2.5 Focus in the detector plane

Rays coming from the source are directed towards the two elliptical mirrors, but not all the rays, reaching the detector plane, are of interest. In ray tracing we divide rays on 'good' and 'bad'. 'Bad' rays are all those, which propagated over the surface without intersection or arrived below the optical surface. The rays, which are reflected by the surface of an optical element, are called 'good' rays. For the case of several mirrors 'good' rays should be reflected by all mirrors before they are detected. The resulting beam is filtered in a way to comprise only 'good' rays, and such rays form the focus spot on the detector.

3.2.2.6 Entrance pupil and solid angle

For the microscopy application we are interested to capture as much light as possible. We use entrance pupil as a factor of merit. The 'good' rays, reaching the detector, are traced back towards the source until the intersection with the fixed plane. This intersection plane is located on the half

[2]Degradation of HEW by 100x times is an arbitrary choice for this system.

of the distance between the origin of the coordinate system $[0, 0, 0]$ and the left edge of the first mirror and is always perpendicular to the vector, directed from the origin to the center of M1. The points of intersection with this plane form an entrance pupil distribution.

The entrance pupil data is characterized by the area and the solid angle. The data distribution is a plane quadrilateral, which can be any of a square, rectangle, trapezoid or parallelogram. To calculate the area of the entrance pupil we first find four extreme corner points of the figure ABCD. Each of these figures we divide into two triangles - ABC and ACD. Their sides are calculated from knowing the vertex coordinates. We find the triangle area as $Area = \sqrt{p(p-a)(p-b)(p-c)}$, where a, b, c are triangle sides and $p = (a+b+c)/2$. The area of the entrance pupil ABCD is a sum of the areas of the two triangles ABC and ACD. The solid angle is simply calculated as area of the entrance pupil divided by half the distance between $[0, 0, 0]$ and the left edge of the first mirror (point belonging to the intersection plane) squared.

Solid angle of a system is typically found as a ratio of an area on a sphere with radius R and R^2 - $area/R^2$ - and expressed in steradians. In our case, we are dealing not with a circular entrance pupil distribution, but a rectangular one, for which solid angle is usually calculated differently. However, for the optimized KB system (see Section 3.4) the entrance pupil area is of around a few mm^2 while the surface area of a corresponding sphere is of order of 0.2 m^2. Thereby, for such a small spot of a spherical surface we can assume that circular and rectangular entrance pupils provide very similar solid angles. Hence, for rectangular pupil we use the formula mentioned above.

3.2.2.7 Assumptions and constraints

There are several constraints which apply to our system. Some of them are defined by properties of X-ray radiation and some are the requirements of the desired X-ray microscopy setup.

- High-energy radiation puts its constraints on the grazing angle of the reflecting optics. The angle should be very small. For a reflectivity of around 50%, grazing angle on a surface of a Silicon wafer is approximately 4.5 degrees for X-rays of energy 100 eV, around 1.6 degrees for 1 keV and less than 0.2 degrees for 10 keV X-rays [24]. The grazing angle on the first mirror is an input parameter of the system and can be controlled. At the same time, ensuring the grazing incidence

on the second mirror within the accepted range is crucial for the high performance;

- We are interested in producing magnified images of the object. The desired magnification is at least 20 in one direction;
- The desired X-ray microscopy setup is of room size (SF $<$ 5 m).

3.3 Modelling method

3.3.1 X-ray tracing python package

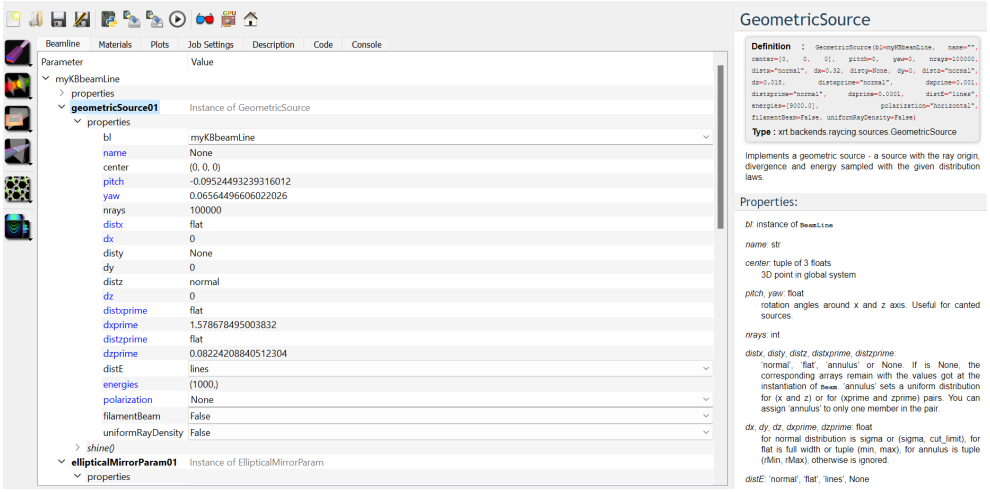

Figure 3.4: *Look of the graphical user interface xrtQook, where the optical system can be created.*

For this project we decided to search for the existing tools to perform modeling of the system. The solution was found in the python-based package XRT (XrayTracer) [25] written by Konstantin Klementiev (MAX IV Laboratory) and Roman Chernikov (Canadian Light Source) specifically for X-ray application. This library contains an extensive range of possibilities to create and investigate a customized optical system. The XRT package requires some additional tools to be installed before the use (e.g.pyopencl, PyQt5, PyOpenGL and PyOpenGL_Accelerate). The full list can be found on the website of XRT.

The setup can be created using the graphical user interface called xrtQook (see Figure 3.4). The user can choose the source (e.g. geometrical source, undulator, wiggler, bending magnet), optical elements (e.g. mirror, crystal, lens, zone plate, etc.), materials, apertures and screens. The various parameters of the corresponding element (such as position, orientation angles, beam energy, size, etc.) can be changed. When the system is created, it can be visualized in an interactive 3D viewer xrtGlow (see Figure 3.5). The parameters of the system can be varied during the viewer is open and will be shown immediately. It is also possible to generate and save a python script, describing the drawn up system. The script allows to control the system in a more precise and automated way and allows for the further investigation and analysis of the results.

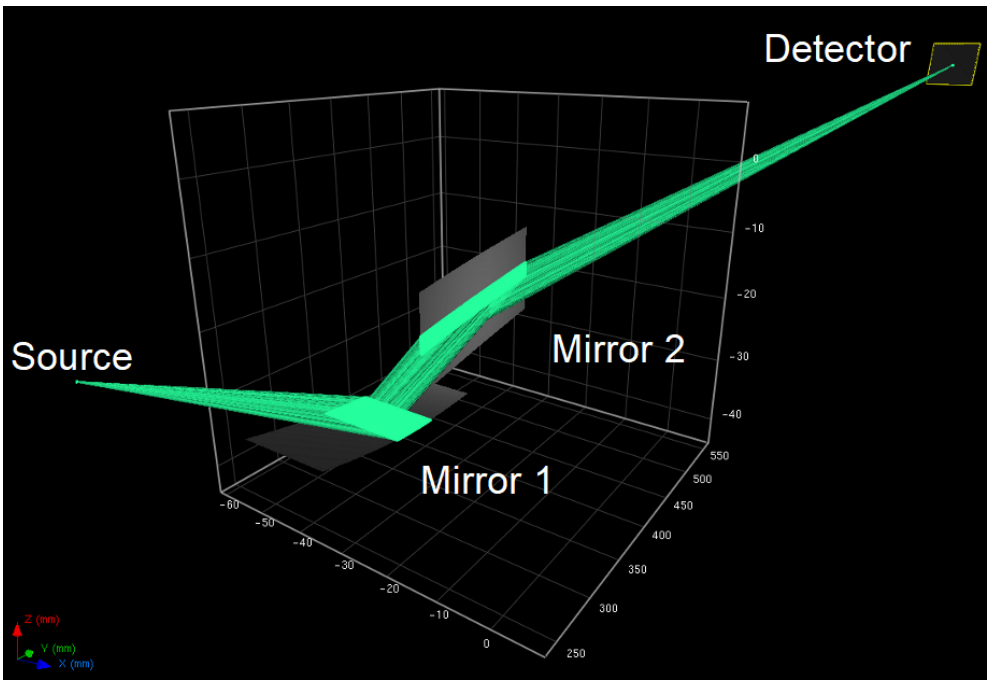

Figure 3.5: *Visualization of the KB system, created with xrtQook interface, in an interactive 3D viewer xrtGlow.*

Specifics of the generated code and input parameters

For the KB optical system we require a point source. It is set by *GeometricSource*() function, and for the point source parameters dx, dy, $dz = 0$ (size of the source). Besides that we choose other parameters of the source: *source_center*, *source_pitch* (rotation around x) and *source_yaw* (rotation around z). Diver-

gence angle of rays is set by *dxprime* and *dzprime*, distribution of diverging rays *distxprime*, *distzprime* is 'flat' (uniform).

The optical elements of KB system are two elliptical parametric mirrors *EllipticalMirrorParam*(). The corresponding ellipse is defined by two foci f1 and f2 (which coincide with *source_center* and *detector_center*) and by the point, belonging to the elliptical curve and being the center of each mirror (*M*1_*center* or *M*2_*center*). The correct orientation is set by rotation angles around X-, Y- and Z-axis - pitch, roll and yaw - in the corresponding *rotationSequence*. For cylindrical surfaces (with sagittal radius = 0) argument $isCylindrical = True$. The size of the cylindrical elliptical mirror along X- and Y-axis is set by $limPhysX$ and $limPhysY$. The plain screen is defined by *Screen*() with the position *detector_center*.

All elements of the beamline are stacked into the *build_beamline*() function and then are used as anchor points of the ray tracing process. As a result of ray tracing, after each element of the beamline the associative array[3] is created. Each of these objects contain the output arrays (such as starting points, normalized vector directions, energy, etc.) of a beam at a certain moment of ray tracing. The beam going from the source is created by *geometricSource.shine*() function. This beam is further used as an input argument of *EllipticalMirrorParam.reflect*() function which calculate global and local beams reflected from the surface. Similarly, these rays are used as input arguments for the next surface and so on. The final beam rays become the argument of the *Screen.expose*() function. It is important to make sure that the correct beams are going to the correct elements throughput the system. The result of ray tracing at any point can be plotted, saved and analyzed.

3.3.2 Building the wrapper code

The code generated by xrtQook is working with only one set of parameters set by specific values. By further customization we are able to make the code more advanced and automated.

First, the home-made code is created to calculate the output parameters, fully defining the system, by setting the input parameters mentioned in Section 3.2.2.2.

The next step of the code customization is merging the XRT generated code with the home-made code written for calculating the parameters of the optical system. Instead of one set of values, we set the arguments of

[3] An associative array (dictionary) is an abstract data type holding data in (key, value) pairs.

XRT functions as variables and, hence, acquire more control over the code. Such an approach reveals an infinite number of possibilities to investigate the optical system. For example, a sensitivity study can be run to find the optimal parameters to fulfill the desired output of the system.

3.4 Optimization of parameters

This section is devoted to exploration of the parameter space of the KB system. For this we conduct a sensitivity study and see how sensible are the output parameters to some of the system entry parameters. The deliverables we look at are tightness of focus in the form of half-energy width, throughput (% of good rays that make it through the system while reflecting from both mirrors), solid angle and curvatures of the mirrors. The divergence of a source stays fixed throughout the exploration. Table 3.1 presents a summary of parameter space exploration.

	HEW	**% good rays**	**Solid angle**	**Curvatures**
Grazing angle	increases	increases	increases	decrease
System length	increases	decreases	decreases	increase
Dist. b/w mirrors	decreases	decreases	decreases	increase
Magnification	decreases	increases	increases	decrease
Mirror length	has optimum	increases	increases	increase

Table 3.1: *Table presents the results of sensitivity study. The first column shows the varying parameters (one at a time, the rest are fixed). The first row shows the parameters for the assessment of system performance.*

As we increase grazing angle from 0.5 to 2 degrees, throughput (for a fixed divergence of the source) and solid angle of the system increase from 0.1 to 2.1% and from $7.87 \cdot 10^{-5}$ to $5.76 \cdot 10^{-4}$ sr, correspondingly. However, half-energy width of focus distribution increases from $4.02 \cdot 10^{-5}$ to $2.55 \cdot 10^{-3}$ mm. In addition, the estimated curvature of the first mirror decreases from around 52 m to 12 m, which is less suitable but still acceptable for manufacturing.

When gradually increasing the system length from 2.5 to 50 m, we observe the worsening of almost all the output parameters. HEW increases from $6.39 \cdot 10^{-5}$ to $1.31 \cdot 10^{-3}$ mm, percentage of good rays drops from 0.83 to 0.003% and solid angle decreases from $2.27 \cdot 10^{-4}$ to $2.02 \cdot 10^{-6}$ sr. As expected, the bigger system allows for the manufacturing of flatter mirrors: the radius of curvature of mirror 1 increases from 22 m to 453 m. Note

that under fixed magnification for each of the varying system lengths the distance between the source and mirror M1 changes such that the ratio of distances M1-detector and source-M1 remains constant, as follows from the definition of magnification.

Let us now vary the distance between the mirrors, specifically between the right edge of M1 and the left edge of M2 (along the Y-direction). We increase this distance by shifting the center of the second mirror further from the source. The distance is varied from 0 (mirrors touch) to 300 mm between the mirror edges. Since the first mirror does not move, its radius of curvature remains constant around 45 m. The curvature of the second mirror grows from 106 to 209 m. Throughput and solid angle of the system decrease from 0.19 to 0.08 % and from $9.71 \cdot 10^{-5}$ to $3.64 \cdot 10^{-5}$ sr, correspondingly. The focus gets slightly better, decreasing from $5.62 \cdot 10^{-5}$ to $4.42 \cdot 10^{-5}$ mm. We are interested in producing the image, magnified roughly equally in both horizontal and vertical directions. The magnification is estimated as the ratio of distances between the center of the mirror and detector and between the center of the mirror and source. The approximately equal magnification in both planes implies that the distance between mirrors should be less as possible (but for physical reasons it can not be equal or greater than the length of mirrors).

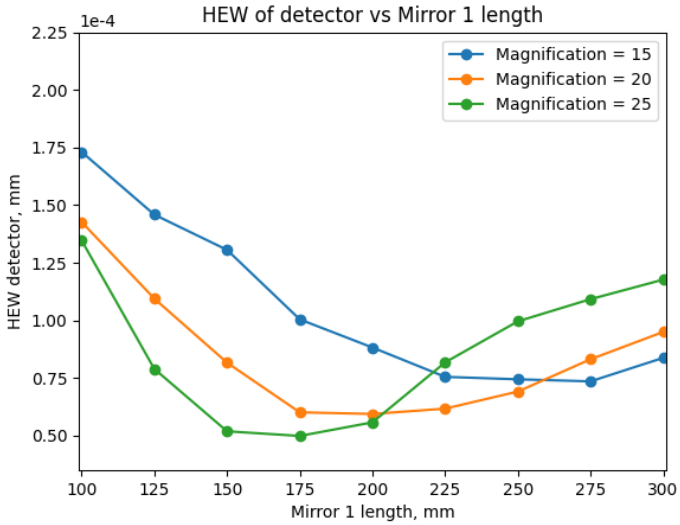

Figure 3.6: *Dependence of half-energy width distance of focus distribution versus varying length L_y of the first mirror for different magnifications produced by the first mirror.*

The last two rows in the Table 3.1 show the dependence of the sys-

tem parameters versus magnification and length L_y of the first mirror. We consider them simultaneously and see their co-dependence. Certain magnification conditions force the specific mirror length: the system has an optimum in half-energy width when varying over the mirror lengths (see Figure 3.6). For example, the system with magnification of 20 has an optimal mirror length of around 200 mm, for the system with magnification 25 the optimum is around 175 mm. Hence, the higher the desirable magnification of the image produced by the first mirror, the shorter the first mirror has to be along the direction of Y-axis. At the same time, when going from magnification of 15 to magnification of 25, focus at the optimal mirror length slowly reduces from $7.53 \cdot 10^{-5}$ to $4.81 \cdot 10^{-5}$ mm.

Under fixed system length, the magnification m_1 constraints the position of the first mirror: the closer it is to the source, the larger the magnification of the system in YZ-plane. The corresponding ellipse, providing the mirror shape, changes accordingly. Since the focal points of ellipse stay fixed, its length and width change, ellipse becomes flatter and more elongated along the optical axis (along Y-axis).

When increasing magnification from 15 to 25, radius of curvature of the first mirror decreases from 59 to 37 m, while remaining the same over the mirror lengths varying from 100 to 300 mm. Curvature of the second mirror decreases for both dependencies. For the magnification fixed at 15, solid angle goes up from around $4.12 \cdot 10^{-5}$ to $8.59 \cdot 10^{-5}$ sr. The trend grows approximately twice these values for the magnification of 25. Note that in the case of these dependencies the solid angle grows not due to the increase of entrance pupil area, but due to reduction of the distance to the first mirror (entrance pupil is taken at half the distance between the source and the first mirror). Similarly to solid angle, the system throughput increases with both the increase of magnification and Y-length of mirror 1.

The optimization results give us the guideline to choosing the optimal system. It suggests that:

1. grazing angle on the first mirror is as small as possible;
2. system is of moderate size. Longer systems do not bring benefit except for flatter plates. At the same time too short systems limit the magnification that can be achieved;
3. edges of two mirrors touch;
4. system can have large magnification. The magnification of the first mirror of 20 and higher is preferred;
5. optimal length of the mirror is given by the specific magnification.

The radii of curvature of the optical surfaces are desired to be as large as possible, ideally around several kilometers, such that the plates are almost flat. This objective comes from the Silicon Pore Optics technology. Special mandrels are used to curve the silicon plates, and it is easier to curve the plates only slightly.

As an example of an optimal system we choose 5 m long system, with grazing angle on the first mirror of 0.01 rad (or 0.57 deg) and magnifications of mirrors of 20 and 10. Lengths (L_y) of both mirrors are 200 mm and widths (L_{x1} and L_{x2}) are 12 and 13.5 mm. The output parameters of this optimal system are half-energy width of the focus distribution $= 5.75 \cdot 10^{-5}$ mm, solid angle of $1.02 \cdot 10^{-4}$ sr and radii of curvature of the first and second mirrors are around 45 m and 106 m, which correspond to sag distances of 0.11 and 0.06 mm.

The results of modeling suggest that there is no limit for magnification of the first mirror. At the same time, higher magnification means that the optics moves closer to the source, and at some point it is going to be unphysically close. In addition, higher magnification leads to decrease of optimal mirrors length. The bottom constraint on the mirror length, coming from the SPO technology, is 20 mm.

For a simple KB system, it is unavoidable that magnification of image in the two perpendicular directions are different. For advanced KB system (almost) equal magnifications, produced by the two mirrors, can be achieved by choosing the specific sequence of 2 horizontal and 2 vertical mirrors.

3.4.1 Imaging properties

This section discusses imaging properties of an optical system based on the assessment of field of view and spatial resolution.

Field of view

There several aspects that can introduce degradation of the image quality: degradation of half-energy width of the detector distribution or degradation of system throughput (how many photons are reflected by the system and reach the detector). In our case throughout of the system does not have a strong dependence on the shifting of the source and stays on the same level. At the same time the HEW degradation kicks in very fast.

Figures 3.7 show HEW of focus distribution versus the distance by which the source is moved from origin along the X-axis (top) and Z-axis

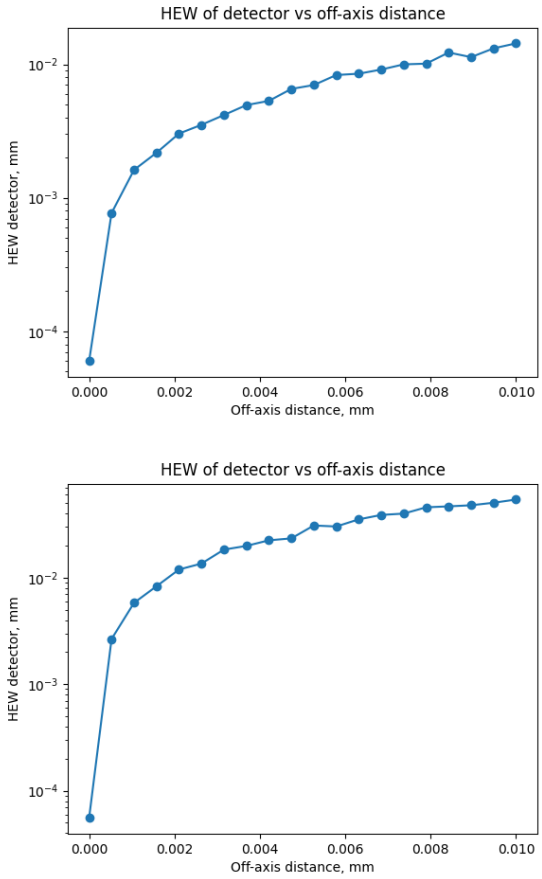

Figure 3.7: *Dependence of half-energy width distance of the distribution in the detector plane versus off-axis distance of the source with shift along X-axis (top) and Z-axis (bottom). Vertical scales are logarithmic. The plots suggest field of view of around 4 μm (top) and 1 μm (bottom).*

(bottom). The vertical axis, presented in logarithmic scale, reveals dramatic increase of HEW already within the first 10 μm of shift in both cases. For the shift along X-direction, the initial half-energy width of $5.81 \cdot 10^{-5}$ mm with source in the origin goes up by 10x within the first 0.5 μm of shift and by 100x within 4 μm. Taking the degradation of the focus by 100x times acceptable within the field of view, we get FOV_x of the system $= 4$ μm. For the case of shift along Z-axis, HEW increases from $5.55 \cdot 10^{-5}$ mm to $5.80 \cdot 10^{-3}$ mm within the field of view, where $FOV_z = 1$ μm.

Figure 3.8 presents the examples of focus distributions for different positions of a source. The source, positioned at origin of the coordinate system (top plot), provides a tight focusing distribution (HEW of $5.81 \cdot 10^{-5}$

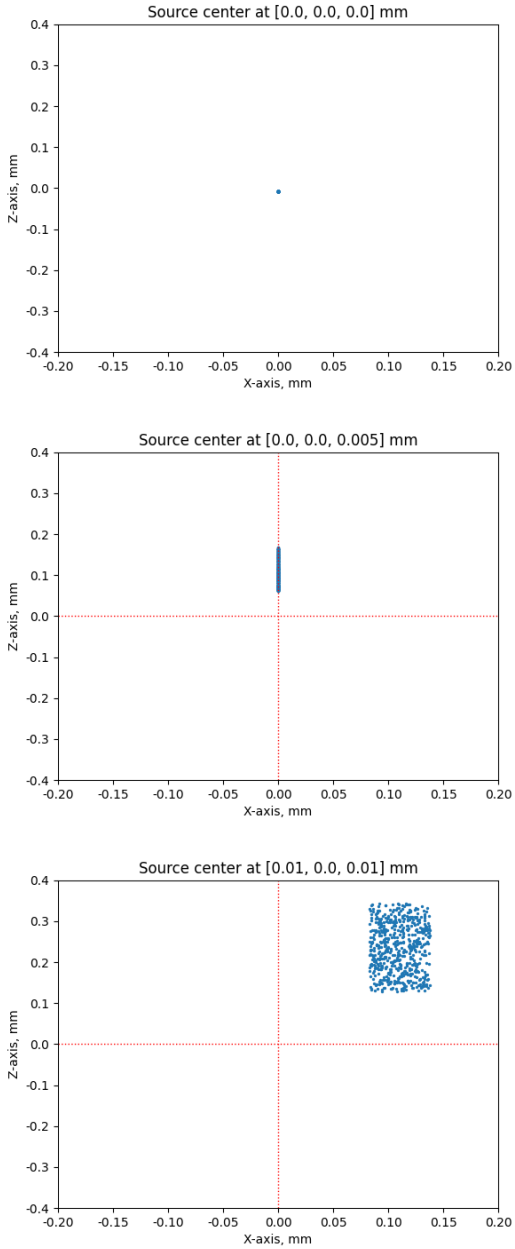

Figure 3.8: *Examples of the focus distribution in ZX-plane of detector for different source positions: source at origin (top), 5 μm shift up along Z-axis (middle), 10 μm in the positive direction of Z- and X-axes (bottom). The red lines in the middle and bottom figures mark the position of the source at origin.*

mm). Middle plot shows that, when the source is moved by 5 μm from the

origin along Z-axis, the vertical dimension of the distribution widens and its center shifts by a value of around 100 μm (in accordance with magnification of 20 of the corresponding mirror). When the source is shifted from the origin by 10 μm along both Z- and X-axis (bottom plot), we see similar behavior: both horizontal and vertical dimensions of the distribution become bigger (HEW is $5.53 \cdot 10^{-2}$ mm) and the center of the distribution shifts along Z- and X-axis by the values according to the magnifications of the corresponding mirrors (20 and 10).

Resolution

Resolution is an important characteristic of an optical system, which shows the ability of the system to distinguish between the objects lying close in the detector image. For the systems, based on the principle of total external reflection, the diffraction limit can be assessed theoretically from the critical angle. We can use the following approximation for the critical angle [20, 26]:

$$\theta_{cr}[rad] = 1.6 \cdot 10^{-2} \cdot \lambda\sqrt{\rho}, \tag{3.4}$$

where λ is wavelength of X-ray light and ρ is reflective material density in g/cm^3. Hence, maximum possible resolution can be calculated as [20, 26]:

$$(D_{diffr})_{max} = \lambda/(2 \cdot sin(\theta_{cr})). \tag{3.5}$$

For silicon mirror plates with density of $2.33 g/cm^3$ and X-rays of $\lambda = 1.24$ nm, critical angle is around 0.03 rad and the maximum achievable resolution is approximately 20.48 nm. For cylindrical mirrors, however, we also need to account for aberrations, which can be theoretically estimated using formula [20, 27]:

$$D_{ab} = \frac{(3m_1 + 7)L_y}{(2m_1 + 2)R_1} + \frac{FOV \cdot L_y}{R_1 sin(\xi_1)}, \tag{3.6}$$

where m, L_y, R are magnification, length along optical axis and radius of curvature of the mirror, ξ is a grazing angle on the mirror, FOV is a field of view of the system. In case of the mirror with $m_1 = 20$, $L_y = 200$ mm, $R_1 \approx 45,000$ mm, $\xi_1 = 0.01$ rad and $FOV \approx 0.004$ mm, contribution of aberrations result in value of 1.42 nm. Total diffraction limit can be calculated as:

$$D_{total} = \sqrt{D_{diffr}^2 + D_{ab}^2} \tag{3.7}$$

and equals to $\sim$ 20.53 nm. This number shows the ideal theoretical resolution of our system. Now let's compare this value to an experimental estimation using the experimentally obtained value of the solid angle.

The optical KB system has a near rectangular shape of an entrance pupil. As it was discussed in Section 3.2.2.6, for the case of an optimal system, providing very small (a few mm^2) area of pupil, we assume the proximity of rectangular and circular shapes of an entrance pupil and consider a resolution formula given by the Rayleigh criterion [28, 29].

The Rayleigh criterion gives a value of a minimum distance, at which it is still possible to separate two sources, as:

$$D_{Rayleigh} = \frac{1.22\lambda}{2 \cdot NA}, \tag{3.8}$$

where λ is a wavelength of light, NA is numerical aperture and 1.22 comes from the definition of Bessel function of the 1^{st} kind (1^{st} minima of the diffraction pattern appears at 1.22 units from the central zero). Numerical aperture is a measure, characterizing the acceptance angle of light incoming to the optical system, and can be calculated as:

$$NA = n \cdot sin(\theta), \tag{3.9}$$

where n is refractive index of medium where light is propagating (for X-rays for most materials $n \approx 1$) and θ is a half-acceptance angle of the system.

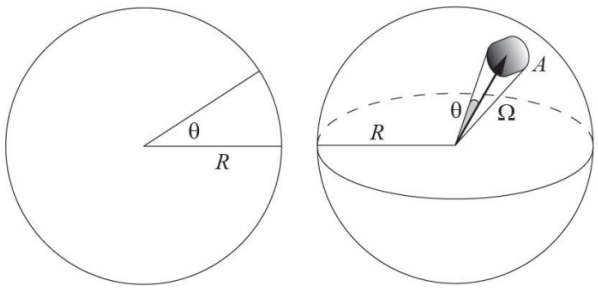

Figure 3.9: *An illustration of analogy between 3D solid angle and 2D half-acceptance angle. Credit: [30]*

Assuming that solid angle Ω forms approximately a cone with half-apex angle θ, we calculated it as [30]:

$$\Omega = \frac{Area}{R^2} = 2\pi(1 - cos(\theta)), \tag{3.10}$$

where $Area = 2\pi R^2(1 - cos(\theta))$ is an area on a sphere with radius R (see Figure 3.9). Expressing angle θ in terms of solid angle Ω, we find numerical aperture as:

$$NA = n \cdot \sqrt{1 - (1 - \frac{\Omega}{2\pi})^2}. \tag{3.11}$$

The numerical aperture of the system is calculated to be approximately 0.0055. Hence, the experimental estimation of a resolution, the considered optimal system can provide, is around 135 nm, which is worse than the theoretical estimate of around 21 nm, calculated earlier.

Chapter 4

SPO stacks for KB system

4.1 Introduction

In the previous chapter we have studied the traditional Kirkpatrick-Baez system based on the two reflections from the elliptical mirrors. Going forward we would like to understand whether it is possible to increase the collection area and solid angle of the system using stacks of multiple reflecting mirrors. First, we discuss the Silicon Pore Optics (SPO) technology, which enables production of the mirror stacks. Second, we consider the possibility of using the SPO stacks as an optical element of KB system in the application of X-ray microscopy.

4.2 SPO technique and manufacturing

Silicon Pore Optics technique makes use of super-polished silicon wafers to build focusing mirror stacks for X-ray radiation [12, 31]. The most commonly used wafers, produced with superb quality for a modest cost, have diameter of 300 mm and thickness of 0.775 mm.

SPO technology has the following steps. First, the excessive material is cut away from the wafer, thereby producing a ribbed pattern on one side of the plate (see Figure 4.1). The other side is reflective and left untouched. Further, the wafer is cut into rectangular plates with the ribs along the direction of propagation of the X-rays.

Subsequently, all plates are subjects to wet-chemical etching. The wet-chemical processing produces a wedge-like profile along the rib direction. Hence, the ribs plane is at a wedge angle with the reflective side of the

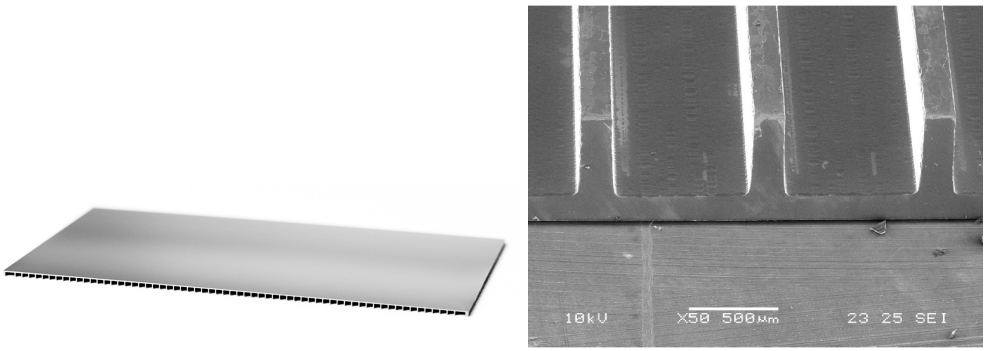

Figure 4.1: *A mirror plate, cut out from a silicon wafer, with a reflective side facing upwards (left). An image of the ribbed side of the plate obtained with scanning electron microscope (right). Credit: [31].*

subsequent mirror plate. This process ensures that the plates, stacked together, will focus X-rays to the same point.

Finally, the plates are stacked together. The mandrel is used to define a shape of the surface of an optical element. The plates are bonded together by a direct bonding property of silicon. The resulting construction, shown in Figure 4.2, consists of multiple pores, the inner walls of which reflect X-rays and guide them to the focal point. The reflective properties of SPO plates can be increased using thin-film coatings of, for example, iridium on top of the silicon wafer surface. The coating is applied in a patterned way via optical lithography in order to still allow the direct bonding of the silicon plates.

The resulting stacks can be used as a reflecting unit, able to collect spatially broader range of X-ray light. It can be also used as a self-supporting stack, where only the top plate is reflective and the rest plates help to maintain the shape.

Figure 4.2: *A mirror stack produced with Silicon Pore Optics technology. Credit: cosine.*

4.3 Description of a multi-shell KB system

Multiple mirrors, located one under another, are typically used to increase the area to collect photons. This mechanism is called 'nesting', and the mirrors are called 'shells'. From now on we refer to a stack as a multi-shell system.

4.3.1 Theoretical principles of building a stack

The ideal multi-shell system is based on a set of confocal ellipses, which all share the same focal points S and F (see Figure 4.3). Focal distance c is the same for all of them, while half-length a and half-width b differ for each ellipse. Similarly to the description of a single-shell system, each of the reflecting plates is a segment of a corresponding ellipse. We consider the first (upper) shell to have the same settings as for the single-mirror system.

Building of an effective stack requires taking into account the fact of shadowing. Some part of the light coming from the source is not going to pass through the system of shells towards detector. As shown in Figure 4.3, for the second and subsequent shells the effective reflecting area is shrinking. Part of the incoming from the sample light is blocked by the left edge of the upper shell. Moreover, not all the rays are further reflected to the detector plane, part of it is blocked by the right edge of the upper

mirror. Following this principle, we choose the parameters of the shells such that the area of the mirror is equal to effective reflecting area and does not produce an excessive blocking of light for the lower shells. Utilizing these conditions allows to construct an ideal stack without the hindrance like the effect of shadowing.

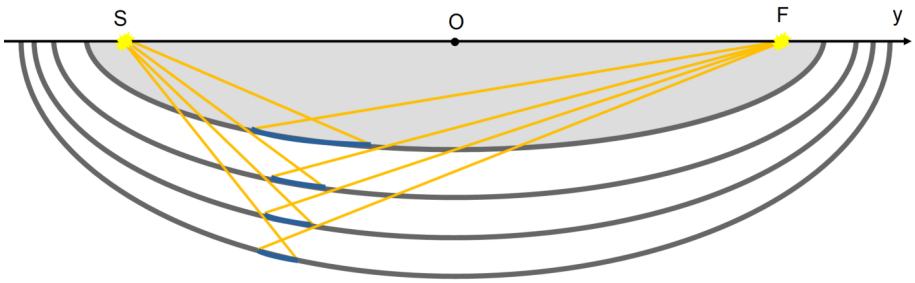

Figure 4.3: *Ideal system of the confocal ellipses sharing the same foci points S and F. Yellow rays show the principle of formation of the effective elliptical mirrors lengths (blue) when taking into account the effect of shadowing.*

Besides the lengths, mirrors also differ by a pitch angle because they belong to different ellipses. Difference between pitch angles of shells number n and $n+1$ gives a wedge angle between the plates. The wedge angle is found separately for each pair of shells.

One can imaging that production of an ideal confocal stack of mirrors is difficult. It is so not only due to the need of producing mirrors of different curvatures just for one stack (mandrels of high-quality are typically very expensive), but also stacking them further together is problematic. Plates in a stack are held together by the direct silicon bonding process. Stacking two plates of different curvatures means that they will have less points of contact and, hence, less possibilities to be 'glued' together. Stacking many plates in such way may significantly affect the rigidity and reliability of a multi-shell system. For these reasons we are interested in manufacturing of an 'averaged' stack, which parameters are averages over the calculated ideal lengths, curvatures and wedge angles of mirrors. We can undoubtedly expect that the stack with averaged elements will perform worse than the ideal stack would. However, the less the initial difference there is between the ideal individual lengths/curvatures/wedge angles, the more subtle degradation of the performance will be.

4.3.2 Modelling of the multi-shell stack

X-Ray Tracer allows to simulate non-sequential propagation by looping over individual mirrors and merging rays into a single "Beam" object. For each of the mirrors parameters are calculated separately. The function *calculate_mirror_parameters* calculates initial output parameters of mirror 1 (center, pitch, yaw) and ellipse (a and b). These are later used to find other parameters of the first and other shells using $calculate\_new\_shell()$.

Function $find\_number\_of\_shells()$ is used to find number of shells and their lengths. To do this, we find an intersection of the two vector rays with ellipse (see Figure 4.3). The first ray goes through the origin (0, 0, 0) and the left edge (along Y-axis) of the first shell. The second ray goes through the detector point (0, 2c, 0) and the right edge of the first shell. Note that in this case it suffices to work only with projections on YZ-plane. To find the length of the second shell, we calculate the intersection points of rays 1 and 2 with the ellipse of this shell. The optimal Y-length of the second shell is the difference between the Y-coordinates of the two intersection points. Taking into account large radius of curvature of the ellipse and small ellipse segment, we assume the mirror length is equal to its Y-projection.

The length of the first shell (L_{y1}) is an input parameter and can be varied. Modelling shows that the length of each subsequent shell is less the previous one ($L_{y1} > L_{y2} > L_{y3} > ...$). Hence, the larger L_{y1}, the more shells stack can have. In the ideal case of confocal ellipses the center of each subsequent shell shifts closer to the source along Y-axis.

Example

Let us consider an example of a stack modelling given the optimal parameters found in Section 3.4:

- System size - 5 m;
- Grazing angle on the first mirror - 0.01 rad (0.57 deg);
- magnification - 20;
- mirror's length L_y - 200 mm;
- distance between centers of M1 and M2 equals to L_y.

The silicon wafers, which are most commonly used and have the highest quality of the surface, are of 300 mm diameter and have 0.775 mm thickness. The diameter brings in a limitation on the mirrors' lengths,

they, hence, can not be longer than 250 mm. Thickness of wafers fixes the distance between the shells in a stack and therefore the height of each pore.

The modelling gives the following result. For the above mentioned optimal parameters stack can only have one shell with the parameters coinciding for a single-mirror system. Increasing the mirror's length L_y to 250 mm we get two shells. Center of the second shell is shifted by 34 mm to the left along Y-axis. Wedge angle between the mirrors is 0.004 rad or 825 arcsec. Plates lengths are correspondingly 250 and 1.4 mm. Mirrors radii of curvature are 45 and 90 m. The second shell does not bring anything to the system - it is not realistic to consider a mirror shorter than 20 mm.

By further increasing the mirror length (beyond the wafer constraints) up to 350 mm, it is possible to model a stack with three shells, which centers along Y-axis are at 238, 177 and 167 mm, accordingly. Lengths of shells are 350, 136 and 63 mm, radii of curvatures are 45, 68 and 87 m. The wedge angles are 0.0054 rad (1114 arcsec) and 0.0022 rad (454 arcsec).

Conclusions about the stack relevance

The results of a modelling example show that the requirements of the stack are not compatible with the requirements for the room-sized microscopy setup. Let us consider several aspects leading to such a conclusion.

1. Modelled stack does not satisfy the minimal number of shells in a stack. For the considered examples we obtain maximum 1-3 shells, while a self-standing stack requires at least 7-8 plates to be able to hold together and maintain the shape imposed by the mandrel.

2. Wedge angles are enormously big for the stack production. The acceptable range of angles is less than 10 arcseconds (for Wolter-1 design in ATHENA this number is around 3 arcsec). In our case this number is at least 400 arcsec, which is not possible to produce using SPO technology and wet-chemical etching.

3. Plate lengths change very rapidly. For production we are interested in mirrors of the same length to be stacked together. To find an optimal length of the mirrors in stack we need to average over the lengths of the ideal set of mirrors. However, in our case the plate's length reduces approximately 2x times for each next shell, making

it difficult to find an optimum. Taking the average length automatically blocks the possibility of reflection for the mirrors with smaller 'ideal' length.

4. Rapid change in radii of curvature between subsequent shells. It does not seem relevant to average over the curvature. Such averaging will worsen the final performance too much.

5. Possible usage of stack does not bring increase of gain in the solid angle. The bigger solid angle can be achieved with just one longer first plate than a stack.

From this we draw a conclusion that it is hardly possibly to build and achieve good results using a stack of silicon mirrors in the case of microscopy. Diverging rays coming from the source of fluorescence lead to an excessive shadowing (hence, big wedge angles and small number of shells), and the resulting parameters are not compatible with requirements for SPO stack production.

This conclusion applies also to the case of advanced KB system with four mirrors. In order to get high magnification, the optics needs be placed close to the fluorescent source (closer than for a simple KB system because due to additional mirrors the resulting distance between optics and detector reduces). This implies large change of grazing angles from plate to plate and results in very different pitch angles, impossible wedge angles and lots of shadowing.

4.4 KB stacks for infinite-distant source

In the previous section we found that SPO stacks in KB configuration are not relevant to be used for the source with diverging beam. Nonetheless, it was reported by Willingale and Spaan in 2009 [32] that the KB stacks can be used successfully for a source at infinity with (almost) parallel rays.

The authors propose to use stacks of flat wedged plates in orthogonal KB configuration. A pair of such perpendicular stacks makes up one optical module and provides a fraction of the total collection area. Combining multiple mirror modules together, using the sunflower filling rule and lobster mirror design (see more details in [32]), allows to achieve maximum collection area and have limitless field of view. Introducing parabolic curvature of the KB plates along the X-ray propagation could possibly improve the resolution (not addressed in the paper).

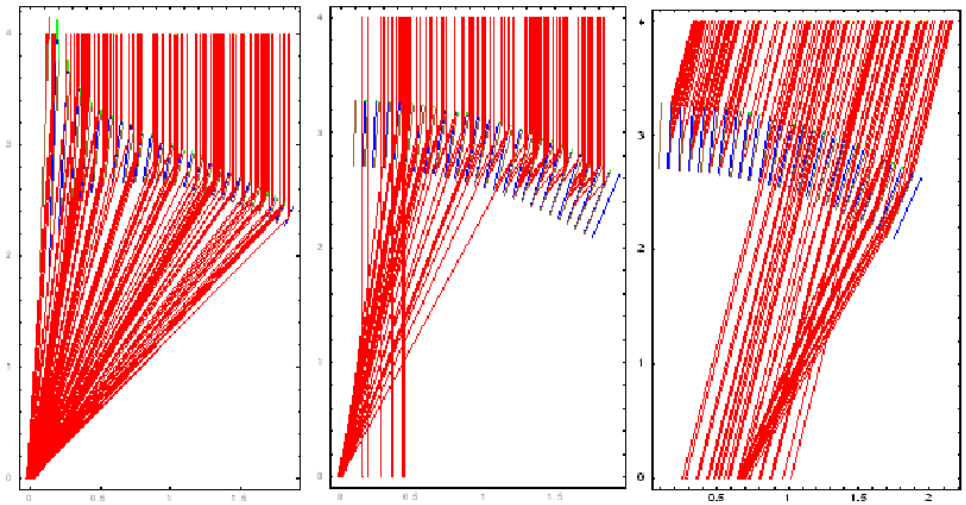

Figure 4.4: *An example of a 2D simulation of 25 mirrors of varying (left) and fixed length (center, right) placed on a part of a circle. Central and right figures differ by the angular position of the light source. Credit: [32]*

Figure 4.4 shows an example of a 2D simulation of 25 mirror plates with their centers distributed along a part of a circle. Left figure presents an idealized system, where plates lengths and rotation angles are optimized for the best focusing of light (taking into account the effect of shadowing). Central picture shows an averaged system, where all plates are of the same fixed length (equal to a quarter of the maximum length in the previous case). As we can see, focusing ability of the system has worsened, some rays are passing through the system without reflection and for some the reflected rays are not passing out of the system. Figure on the right confirms similar behavior for the other angular position of the source.

One can see that for the case of a source infinitely far away (parallel incoming beam) it is possible to model and manufacture reasonably good focusing stacks. Tessellation of such stacks aims to provide large collection area and field of view in addition to sufficiently good angular resolution and can serve as a next generation all-sky X-ray monitor [32].

Chapter 5

Concluding summary and Outlook

This project was devoted to the study of Kirkpatrick-Baez X-ray optics for the case of full-field X-ray fluorescence microscopy and of the possibility to use mirrors stacks, made with Silicon Pore Optics technology, to increase the collection area and solid angle of such an optical system.

The X-ray radiation is highly energetic, and with its advantages it also brings the challenges, for example, in focusing. The existing X-ray focusing problem is commonly solved by utilizing the principle of total external reflection at grazing incidence. The X-rays are falling on a sufficiently dense surface at a small grazing angle and are reflected. There are several designs developed for the efficient focusing of X-rays. The most popular Wolter-1 type is used for an optical system in ATHENA telescope. However, Wolter optics is not possible to manufacture with high quality for microscopy setup. The Advanced Kirkpatrick-Baez design is an interesting candidate for its replacement: it combines benefits of Wolter optics design and relative cheapness and ease in manufacturing inherited, from a simple Kirkpatrick-Baez system.

In this thesis we conduct a study of KB system of two reflecting elliptical mirrors. System of two KB mirrors is not a proper imaging system and mostly used for scanning type of microscopy. Even so, it is a stepping stone and basis for the further development of a full-field X-ray microscope, which uses system of four KB mirrors (Advanced KB) and combines benefits of both Wolter and KB systems. The conclusions drawn from the simple KB are fully applicable to an advanced KB optical system.

Many papers present the results of study of KB design but not one of them unfold the detailed equations needed to model the system. The required equations for a system of two elliptical mirrors in KB design were derived as a first step of investigation. Using modelling tool such as Ze-

max allowed to get a first feeling of the system and helped to confirm the correctness of the derived equations. However, functionality of Zemax was not enough to perform the data analysis required for thorough understanding of the optical system. Switching to X-Ray Tracer (XRT) allowed to get access to an extensive python based tool. With XRT it is possible to construct an optical system and use the generated python code for ray-tracing and data analysis.

Based on the derived equations, optical system was parameterized and characterized. Performance was assessed on the basis of solid angle, throughput of the system and half-energy width of the focus distribution in the detector plane. By alternately fixing and varying some of the input parameters we explored the parameter space and established the requirements for developing of an optimal system. Optimal system is of moderate size and have magnification of the first mirror of at least 20. Interestingly, system magnification enforces a specific mirror length, at which the HEW of focus is the smallest. In addition, grazing incidence on the first mirror is preferred to be as shallow as possible, and the edges of two mirrors touch each other.

For the example of an optimal system we performed ray tracing and obtained the results of modelling. In addition, we confirmed that the imaging properties of the system are not of the best quality. As the source is moved off-axis, the image quality degrades fast due to the degradation of focus HEW. For this specific system we choose an arbitrary, acceptable within the field of view, degradation of 100x times. The resulting fields of view (from the center outwards) were established to be of order of 4 μm (along X-axis) and 1 μm (along Z-axis).

The main goal of the project was to understand whether it is possible to use a stack of several mirrors in order to collect more photons and increase the solid angle. The principles of constructing the suitable reflecting stack were developed theoretically and further implemented for modelling with XRT package.

Limitations, enforced by the parameters of an optimal system, as well as the constraints, coming from the silicon wafer production and SPO technology, showed that the construction of a SPO stack is not relevant in the case of microscopy, and there are several reasons for it. One of the main aspects is not sufficient minimal number of plates. With just one to three plates it is not possible to build a stack that will rigidly keep the shape imposed by the mandrel. The second critical impossibility is coming from the wedge angles. The modelling shows that the resulting angles between plates are excessively big to be produced with the wet-chemical etching technology. In addition, there is a rapid change over the value of plate

lengths and radii of curvature for different shells. This makes it difficult to establish the optimal value for each parameter, since the averaging over the rapidly varying values will lead to a significant reduction in the system performance. Impossibility to use the benefits of SPO stacks in the set of two KB mirrors leads to a similar conclusion for the case of four-mirror AKB system.

Despite the fact that the SPO stacks are not relevant for the case of divergent source, it was shown by [32] that the system of KB stacks can be used successfully for the case of infinite source with parallel incoming rays.

SPO technology can still provide benefits for the full-field X-ray microscopy based on AKB. With it we can manufacture stacks (with minimum of 7-8 plates) with just the upper plate reflective and lower plates present to maintain the structural shape. It can be a method for a cheap and reliable production of curved mirrors of high quality, e.g. for the AKB optical systems.

Outlook

There are further steps, which can be done as a logical continuation of this research:

- describe and model AKB analogously to as it was done in this thesis for KB system;
- conduct an optimization of parameters and characterize the resulting system;
- study the imaging properties (i.e. resolution, field of view) of the AKB system.

Going forwards into investigating the Advanced KB system will bring us closer to the development of a full-field X-ray fluorescence microscope.

Acknowledgements

This research was made possible by financial support in the from of scholarship from the LUF and the Den Adel Fund.

Bibliography

[1] S. Matsuyama, H. Mimura, H. Yumoto, Y. Sano, K. Yamamura, M. Yabashi, Y. Nishino, K. Tamasaku, T. Ishikawa, and K. Yamauchi. Development of scanning x-ray fluorescence microscope with spatial resolution of 30 nm using kirkpatrick-baez mirror optics. *Review of Scientific Instruments*, 77(10):103102, 2006.

[2] Y. Suzuki, A. Takeuchi, H. Takenaka, and I. Okada. Fabrication and performance test of fresnel zone plate with 35 nm outermost zone width in hard x-ray region. *X-Ray Optics and Instrumentation*, 2010(824387), 2010.

[3] J. Miao, P. Charalambous, J. Kirz, and D. Sayre. Extending the methodology of x-ray crystallography to allow imaging of micrometre-sized non-crystalline specimens. *Nature (London)*, 1999.

[4] Y. Nishino, Y. Takahashi, N. Imamoto, T. Ishikawa, and K. Maeshima. Three-dimensional visualization of a human chromosome using coherent x-ray diffraction. *Phys. Rev. Lett.*, 102:018101, Jan 2009.

[5] T.-Y. Chen, Y.-T. Chen, C.-L. Wang, I. M. Kempson, W.-K. Lee, Y. S. Chu, Y. Hwu, and G. Margaritondo. Full-field microimaging with 8 kev x-rays achieves a spatial resolutions better than 20 nm. *Opt. Express*, 19(21):19919–19924, Oct 2011.

[6] B. Lengeler, C. G. Schroer, M. Kuhlmann, B. Benner, T. F. Günzler, O. Kurapova, F. Zontone, A. Snigirev, and I. Snigireva. Refractive x-ray lenses. *Journal of Physics D: Applied Physics*, 38(10A):A218–A222, may 2005.

[7] S. Matsuyama, J. Yamada, Y. Kohmura, M. Yabashi, T. Ishikawa, and K. Yamauchi. Full-field x-ray fluorescence microscope based on

total-reflection advanced kirkpatrick-baez mirror optics. *Opt. Express*, 27(13):18318–18328, Jun 2019.

[8] M. Hoshino, T. Ishino, T. Namiki, N. Yamada, N. Watanabe, and S. Aoki. Application of a charge-coupled device photon-counting technique to three-dimensional element analysis of a plant seed (alfalfa) using a full-field x-ray fluorescence imaging microscope. *Review of Scientific Instruments*, 78(7):073706, 2007.

[9] P. Kirkpatrick and A. V. Baez. Formation of optical images by x-rays. *J. Opt. Soc. Am.*, 38(9):766–774, Sep 1948.

[10] R. Kodama, N. Ikeda, Y. Kato, Y. Katori, T. Iwai, and K. Takeshi. Development of an advanced kirkpatrick–baez microscope. *Opt. Lett.*, 21(17):1321–1323, Sep 1996.

[11] J. Yamada, S. Matsuyama, R. Hirose, Y. Takeda, Y. Kohmura, M. Yabashi, K. Omote, T. Ishikawa, and K. Yamauchi. Compact full-field hard x-ray microscope based on advanced kirkpatrick–baez mirrors. *Optica*, 7(4):367–370, Apr 2020.

[12] M. Beijersbergen, S. Kraft, M. Bavdaz, D. Lumb, R. Guenther, M. Collon, A. Mieremet, R. Fairbend, and A. Peacock. Development of x-ray pore optics: novel high-resolution silicon millipore optics for xeus and ultralow mass glass micropore optics for imaging and timing. *Proc SPIE*, 01 2004.

[13] W. C. Röntgen. Ueber eine neue art von strahlen. *Annalen der Physik*, 300(1):12–17, 1898.

[14] X. Ying, N. J. Barlow, and M. H. Feuston. Micro-ct and volumetric imaging in developmental toxicology. In Ramesh C. Gupta, editor, *Reproductive and Developmental Toxicology*, pages 983–1000. Academic Press, San Diego, 2011.

[15] D. Attwood. *Soft X-Rays and Extreme Ultraviolet Radiation: Principles and Applications*. Cambridge University Press, 1999.

[16] Living Textbook. Geographic coordinate system, 2022. `https://ltb.itc.utwente.nl/page/491/concept/79661`.

[17] Telescope Optics. Aberrations of the conic surface, 2022. `https://www.telescope-optics.net/conic_surface_aberrations.htm`.

[18] Olympus. Optical aberrations, 2022. https://www.olympus-lifescience.com/en/microscope-resource/primer/java/aberrations/astigmatism/.

[19] Telescope Optics. Wavefront aberrations, 2022. https://www.telescope-optics.net/aberrations.htm#caused_by.

[20] V.V. Lider. Kirkpatrick-baez and wolter x-ray focusing optics (review). *J. Synch. Investig.*, (13):670–682, Jul 2019.

[21] S. Matsuyama, N. Kidani, H. Mimura, Y. Sano, Y. Kohmura, K. Tamasaku, M. Yabashi, T. Ishikawa, and K. Yamauchi. Hard-x-ray imaging optics based on four aspherical mirrors with 50 nm resolution. *Opt. Express*, 20(9):10310–10319, Apr 2012.

[22] Hon. E. Abbe. Vii.âon the estimation of aperture in the microscope. *Journal of the Royal Microscopical Society*, 1(3):388–423, 1881.

[23] H. Wolter. Spiegelsysteme streifenden einfalls als abbildende optiken für röntgenstrahlen. *Annalen der Physik*, 445(1-2):94–114, 1952.

[24] B.L. Henke. Mirror reflectivity calculator, 2022. https://henke.lbl.gov/optical_constants/mirror2.html.

[25] K. Klementiev and R. Chernikov. Powerful scriptable ray tracing package xrt. In Manuel Sanchez del Rio and Oleg Chubar, editors, *Advances in Computational Methods for X-Ray Optics III*, volume 9209, pages 60 – 75. International Society for Optics and Photonics, SPIE, 2014.

[26] A.G. Michette. *Optical Systems for Soft X Rays*. Springer New York, NY, London, 1986.

[27] F.J. Marshall. Compact kirkpatrickâbaez microscope mirrors for imaging laser-plasma x-ray emission. *Review of Scientific Instruments*, 83(10):10E518, 2012.

[28] Lord Rayleigh Sec. R. S. Xv. on the theory of optical images, with special reference to the microscope. *The London, Edinburgh, and Dublin Philosophical Magazine and Journal of Science*, 42(255):167–195, 1896.

[29] T. Salditt and M. Osterhoff. *X-ray Focusing and Optics*, pages 71–124. Springer International Publishing, Cham, 2020.

[30] N. Anderson, P. Prabhat, and T. Erdogan. Spectral modeling in fluorescence microscopy, 2022. https://www.semrock.com/Data/Sites/1/semrockpdfs/web_spectral_modeling_in_fluorescence_microscopy.pdf.

[31] N. M. Barriére, M. Bavdaz, M. J. Collon, I. Ferreira, D. Girou, B. Landgraf, and G. Vacanti. Silicon pore optics, 2022.

[32] R. Willingale and F. H. P. Spaan. The design, manufacture and predicted performance of Kirkpatrick-Baez silicon stacks for the International X-ray Observatory or similar applications. In Stephen L. O'Dell and Giovanni Pareschi, editors, *Optics for EUV, X-Ray, and Gamma-Ray Astronomy IV*, volume 7437, pages 98 – 106. International Society for Optics and Photonics, SPIE, 2009.